OPEN ACCESS
IOP Publishing
Superconductor Science and Technology
Supercond. Sci. Technol. **35** (2022) 104003 (10pp)
https://doi.org/10.1088/1361-6668/ac86ac

Formation and propagation of cracks in RRP Nb_3Sn wires studied by deep learning applied to x-ray tomography

Tommaso Bagni[1,*], Diego Mauro[1], Marta Majkut[2], Alexander Rack[2] and Carmine Senatore[1]

[1] Department of Quantum Matter Physics, University of Geneva, Geneva, Switzerland
[2] ESRF—The European Synchrotron, Grenoble, France

E-mail: tommaso.bagni@unige.ch

Received 6 June 2022, revised 25 July 2022
Accepted for publication 3 August 2022
Published 6 September 2022

Abstract

This paper reports a novel non-destructive and non-invasive method to investigate crack formation and propagation in high-performance Nb_3Sn wires by combining x-ray tomography and deep learning networks. The next generation of high field magnet applications relies on the development of new Nb_3Sn wires capable to withstand the large stresses generated by Lorentz forces during magnets operation. These stresses can cause a permanent reduction of the transport properties generated by residual deformation of the Nb_3Sn crystal lattice as well as the formation of cracks in the brittle Nb_3Sn filaments. Studies for the development of the high luminosity LHC (HL-LHC) upgrade showed that nominal transverse compressive stresses above 150 MPa may be sufficient to generate cracks in the wires. In the case of fusion magnets, wires experience periodic bending due to the electro-magnetic cycles of the reactor which over time may induce wire deformation and filament cracks. Therefore, it has become essential to develop a quantitative method for the characterization of crack formation and propagation under compressive loads. The x-ray tomographic data of a series of restacked-rod-process (RRP) Nb_3Sn wires was acquired at the micro-tomography beamline ID19 of the European Synchrotron Radiation Facility (ESRF), after intentionally inducing a broad spectrum of cracks in the Nb_3Sn sub-elements. The samples were submitted to transvers compressive stresses, with and without epoxy impregnation, at different pressures, up to 238 MPa. The resulting tomographic images were analysed by means of deep learning semantic segmentation networks, using U-net, a convolutional neural network (CNN), to identify and segment cracks inside the wires. The trained CNN was able to analyse large volumes of tomographic data, thus enabling a systematic approach for investigating the mechanical damages in Nb_3Sn wires. We will show the complete three-dimensional reconstruction of various cracks and discuss their impact on the electro-mechanical performance of the analysed wires.

Keywords: x-ray tomography, deep learning, neural network, cracks formation, mechanical limits, artificial intelligence, low temperature superconductors

(Some figures may appear in colour only in the online journal)

* Author to whom any correspondence should be addressed.

1. Introduction

The Nb_3Sn is an A15 intermetallic compound with critical temperature (T_c) of about 18 K [1] and upper critical magnetic field (B_{c2}) up to 30 T [2]. Because of these properties, as well as a high in-field critical current density (J_c), it is the material of choice for superconducting magnets operating above 10 T. Thus Nb_3Sn is used for many applications including: magnet systems of tokamak fusion devices, such as the central solenoid (13.0 T of peak magnetic field) and the 18 toroidal field coils (11.8 T of peak magnetic field) [3] of the International Thermonuclear Experimental Reactor (ITER) [4]; dipoles and quadrupoles accelerator magnets, like the 24 quadrupoles which will be included in the HL-LHC upgrade [5]; magnetic resonance imaging [6]; nuclear magnetic resonance [7, 8]; and laboratory-used high-field magnets including hybrid magnets.

Nb_3Sn is a brittle intermetallic that cannot be drawn in the form of a wire directly. Instead, ductile precursor components are mixed, drawn, and shaped into a final shape (e.g. a coil) before being heat treated, causing Nb_3Sn to form from the precursors by a reactive diffusion process. The production routes for Nb_3Sn vary depending on the type of Nb-alloy precursor and Sn source structure, with RRP and powder in tube (PIT) being those leading to the highest in-field current densities [9]. Being Nb_3Sn a strain sensitive and brittle material, its critical current, I_c, is affected by the applied mechanical loads. In particular, the variation of I_c under loads has two regimes: one reversible, which means that removing the applied load the wire fully recovers from the current decrease imposed by the load, and the other is irreversible, i.e. above a certain irreversible stress limit the current degradation becomes permanent. Two main phenomena are considered responsible for such permanent degradation: the plastic deformation of the Cu matrix, which is always present in the wires, and the breakage of superconducting filaments. The former leaves a residual stress applied to the Nb_3Sn lattice that affects the fundamental superconducting properties of T_c and B_{c2} and consequently the material J_c. The latter reduces the total superconducting cross section and therefore the wire total I_c [10]. The presence of Kirkendall voids, which are created during the reaction heat treatment of the wire, when the Nb–Sn phase forms, also influences the breakage of superconducting filaments. These voids decrease the wire microstructural homogeneity, impacting the wires' mechanical limits, by acting as local stress concentrators and crack nucleation points [11].

Nb_3Sn wires have made great progress in the last 30 years thanks to the ITER research program and, more recently, to the High Energy Physics community due to the development for HL-LHC and for the so called future circular collider (FCC) [12], a higher performance hadron collider capable of reaching collision energies of 100 TeV. Nonetheless, significant step forwards in Nb_3Sn technology are required to meet the current high-field magnet development targets. Wire mechanical tolerances are especially critical because of the large Lorentz forces caused by the high magnetic field and high current on the conductors. In order to produce wires capable of withstanding such stresses, the dominant mechanism causing wire degradation must be identified.

In the case of fusion magnets, cables and wires experience periodic bending due to the electro-magnetic cycle of the reactor [13] and they have to be able to survive tens of thousands of such cycles. Because of the Lorentz force load/unload cycling, the wires suffer from transverse bending and uniaxial strain [14], which may degrade the performance over time due to specific cable-in-conduit conductor design choices [15]. In this frame, several studies showed that the fatigue behaviour and filament cracking are sensitive to wire design and that the filaments are more likely to crack adjacent to Kirkendall voids [16, 17]. On the other hand, in the case of accelerator magnets, studies on the possible configurations for a 16 T dipole for the FCC [18] showed that electromagnetic forces cause large mechanical transverse stresses on the Rutherford cables used to wound the magnets, with peak stress values of 150–200 MPa at 16 T on the Nb_3Sn wires [19]. High performance PIT wires with a diameter of 1.0 mm, developed for the FRESCA 2 dipole at the European Organization for Nuclear Research [20], were tested to evaluate the irreversible degradation as a single wire and assembled in a Rutherford cable made of 18 strands. The plasticization of the Cu matrix was identified as the key irreversible mechanism, establishing the irreversible limit at 110 MPa from the measurement of a single wire with epoxy impregnation [21]. The analysis of the electromechanical tests performed on the Rutherford cable confirmed that plasticization is dominating up to 180 MPa, however above this pressure the filament cracks become more evident and detrimental to the I_c [22]. The key contributor to irreversible degradation in RRP Nb_3Sn wires, on the other hand, was less obvious to identify [23], but the most recent data on electro-mechanical simulation also hint toward copper plasticization as the main mechanism for the I_c reduction [24].

The plasticization of the Cu matrix can be assessed indirectly when a reduction of B_{c2} is measured after mechanical unload of the wire [25]. However, in the case of a macroscopic reduction of the I_c without an alteration in the B_{c2}, the presence of filament crack can be assumed. The latter is then confirmed by metallographic investigation, which usually involves the irreversible destruction of the sample producing few cross sections for scanning electron microscopy [26] analysis. X-ray micro-tomography is a non-destructive alternative to metallography, allowing the study of the internal morphology of a sample, expanding the observable from a few cross-sections to a whole 3D volume. Synchrotron micro-tomography was extensively used to study and characterize the voids formation of Internal-Tin Nb_3Sn wires [27–29]. Furthermore, we have recently integrated this technique with *k*-means, an unsupervised machine learning method, to 3D rebuild the void distribution inside RRP wires [29], culminating in the development of the tomography analysis tool (TAT) [30], a python-based free software for image analysis based on *k*-means [31].

Building on the experience gained during the development of TAT, the goal of the present research is to develop a new approach for detecting cracks in Nb_3Sn wires that combines x-ray micro-tomography with deep learning techniques. This technology will make it possible to perform forensic studies of the wire internal properties enabling the detection of Nb_3Sn filament cracks and their propagation in a non-destructive

way. Thanks to this new tool, researchers will be able to get deeper insights of wire degradation and conceive new approaches for the development of wires with improved tolerance to mechanical loads.

We present here a case study where several RRP samples with and without mechanically induced cracks have been analysed at the micro-tomography beamline ID19 of the ESRF in Grenoble, France, to investigate their internal properties. With a resolution of better than 1 μm pixel^{-1}, the tomographic projections enable a detailed 3D reconstruction of a wire length of about 1.5 mm per scan. The vast volume of data created (approximately 40 GB per scan) is a potential impediment to non-automatized analysis, necessitating the development of new methods to extract quantitative data quickly and reliably. Our approach exploited U-net, a deep CNN [32] for image recognition. CNNs can process large quantity of data providing a nearly human-like precision and allowed us to detect and differentiate features such as voids and cracks in Nb_3Sn wires.

The paper begins with a brief introduction to U-net, the CNN used in the analysis, before moving on to the samples preparation and tomographic data acquisition. The second section is focused on the validation of the CNN for the detection of cracks in RRP Nb_3Sn wires. The final section is dedicated to the discussion of the results and the conclusions.

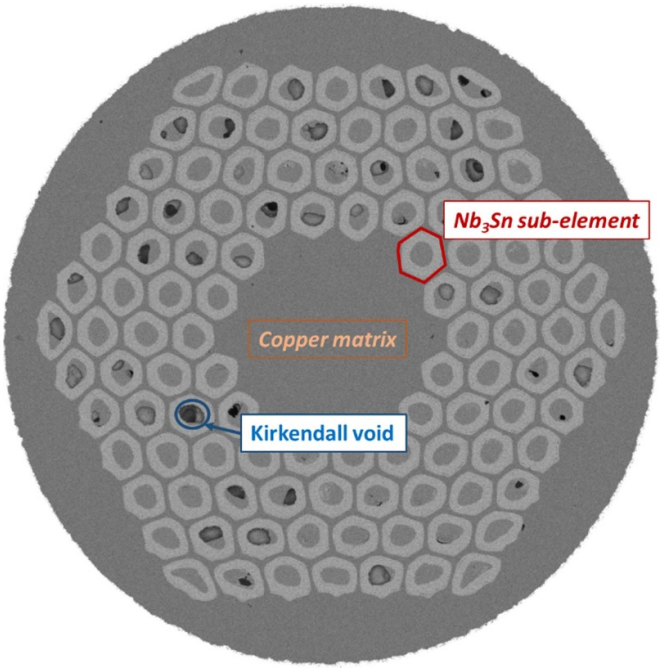

Figure 1. Cross section of the RRP 108/127 Nb_3Sn sample. The wire is 0.7 mm in diameter. The sub-elements are embedded in a high purity Cu matrix, and Kirkendall voids are visible inside some of the sub-elements.

2. Experimental details

2.1. U-net: convolutional neural network (CNN)

In the field of image analysis, neural networks are typically used for classification tasks in which the output is limited to the detection, i.e. the presence or not, of a feature in an image. However, in many visual tasks, such as biomedical applications or our case study, the output should additionally include the localization of the investigated feature, i.e. each pixel that is part of the feature should be labelled. For this, U-net, a fully CNN, was created by Ronneberger *et al* [32].

CNNs are a type of artificial neural network (ANN), which is a computing system inspired by biological neural networks. ANNs are built from a collection of simulated neurons, where each node is linked to other nodes and may exchange signals. Typical nodes are grouped in layers, and the input signals normally pass numerous times across the various layers before reaching the output. CNNs include layers that perform convolutions. A convolution is a linear operation between a weight matrix, referred as kernel, and the 2D image. The convolution is performed by sliding the kernel on top of the image performing an element wise multiplication with the part of the input it is currently on, and then summing up the results into a single output pixel [33]. The weights of the kernel are nearly all zero except around individual pixels which are defined during the training. The kernel repeats this process for every location it slides over, converting the 2D image into a 2D matrix of features. As a result, each convolutional layer only processes data that is relevant to its receptive field, minimizing the number of free parameters and allowing the network to be deeper and quicker than other ANNs [34]. In particular, U-net is a fully CNN, which means that every neuron in one layer is connected to every neuron in another layer allowing the network to receive an arbitrary-size input and produce a corresponding-size output with labelled pixels [35]. U-net gets its name from its U-shaped architecture, which can be separated into two networks: down-sampling and up-sampling. The former network captures the researched features while reducing the spatial information, whereas the latter recreates the input image and assigns each pixel to the predicted category based on weighted probability. The result is an image segmentation, i.e. an output image partitioned into multiple segments or regions.

CNNs, like biological neural networks, require training to learn their tasks and, thus, training is a critical step for the quality of their outputs. Examples are used to train neural networks, which means that a series of inputs and outputs are fed into the network, which then forms an association between the two. Because U-net can segment more than one feature at the time, in the present study we trained it to detect cracks and voids inside the wire, but for other applications, U-net could be trained to segment different wire components like superconducting filaments or specific defects as barrier failures.

2.2. Samples preparation

The present analysis was focused on a RRP wires developed for the 11 T dipoles under development in the frame of the HL-LHC upgrade [36]. The wire configuration is 108/127, with these numbers defining the number of superconducting sub-elements over the total of restacked elements. The wire cross section is visible in figure 1 and the main characteristics of the wire are listed in table 1.

Table 1. Main characteristics of the investigated RRP Nb_3Sn wire.

Billet ID	Wire design	Diameter	Cu/non-Cu	I_c (16 T) (A) I_c (19 T) (A)	Heat treatment
#073A02	108/127	0.7 mm	1.2	185 67	210 °C/48 h + 400 °C/48 h + 650 °C/50 h

Table 2. Main characteristic of the samples processed for x-ray tomography.

Sample name	Experimental setup	Epoxy impregnation	Applied force (kN)	Applied transverse stress (MPa)	Tomographic scan name
S0	—	No	0	0	S0.1
S1	Uni-axial probe	No	1.0	N/A	S1.1
S2	Uni-axial probe	No	2.0	N/A	S2.1
S3	C-WASP probe	Yes	30.0	238	S3.1 and S3.2
S4	C-WASP probe	Yes	30.0	238	S4.1 and S4.2

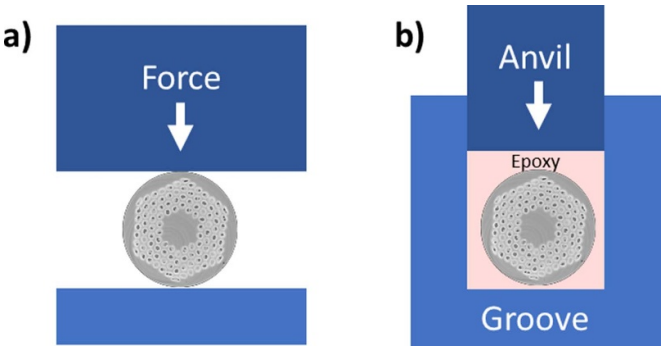

Figure 2. (a) Working schematic of the stress–strain uniaxial setup. (b) Working schematic of the compressive WASP (C-WASP) setup.

Two sets of wire samples were prepared for the analysis. A first set for training and validating the CNN, and the second to evaluate the propagation of cracks in a wire extracted from the measurement probe at the end of an I_c vs transverse stress experiment [23]. The list of examined samples is reported in table 2.

To train and validate U-net was necessary to ensure a set of examples, i.e. tomographic images, showing detectable cracks. To this end we have produced intentionally cracks in the brittle sub-elements of non-impregnated Nb_3Sn wires pressing them between two anvils. Without impregnation, transverse compression of the wire causes pronounced deformation and damage to the wire, leading to the appearance of cracks. Using a setup for measuring the stress–strain relationship of wires subjected to uni-axial loads available at the University of Geneva [23], two bare wires, S1 and S2, were transversally pressed with 1 and 2 kN of force over a length of 15 mm at 4.2 K, the process schematic is shown in figure 2(a). At 1 kN of applied stress, the sample shows mild ovalization, while applying 2 kN the wire was clearly deformed by the flat anvils. Because the contact surface between the wire and the anvil changes with the applied force, it is not possible to accurately determine the transverse stress applied to the samples. A sample S0 with no induced deformation was also created, and its tomographic images were used as a control group for the CNN validation. These samples were utilized to benchmark the network behaviour in absence and presence of cracks.

The second set of tomographic data consists of wire samples S3 and S4 that were extracted from a wire tested in the compressive Walter spring (C-WASP) probe of the University of Geneva. The C-WASP is a setup based on a Walters spring designed to measure the critical current of a resin-impregnated single wire submitted to a transverse force [10]. The sample holder is composed of two parts: a movable lower part with a U-shaped groove in which the impregnated wire sits, and a fixed top part with an anvil that exerts the transverse force on the wire, the schematic of the setup is shown in figure 2(b). More details about the C-WASP probe are reported in [10, 21, 23]. During the C-WASP test, the wire, which was sitting in a 1.0 mm groove, was pressed at 4.2 K with a transverse force as high as 30 kN over a length of 126 mm, resulting in a maximum stress of ∼238 MPa. The equivalent stress is calculated by dividing the applied force by the groove dimension. At 19 T after unloading the force, the measured permanent I_c degradation was 15% of the initial I_c, and a reduction of B_{c2} of ∼0.5 T was also recorded [37]. The latter information indicates that plastic deformation of the copper matrix is present and plays a relevant role in the degradation of the electrical performance of this specific RRP wire. Following the test, the wire, which has an helicoidal shape, was gently extracted from the groove, the epoxy was removed in an acetone bath, and two segments of a length of ∼25 mm that had been subjected to transverse force were prepared for x-ray tomography. Even if the unmounting of the wire from the C-WASP was performed with maximum care, we cannot rule out that some cracks were induced by this process. The tomographic cross sections of the different samples are shown in figure 3.

2.3. *X-ray tomography*

X-ray micro-tomography analyses were carried out at the ESRF's beamline ID19. Synchrotron micro-tomography is a highly effective method for studying the interior characteristics of materials at the μm scale. X-ray micro-tomography was already proven to be suitable for studying the internal

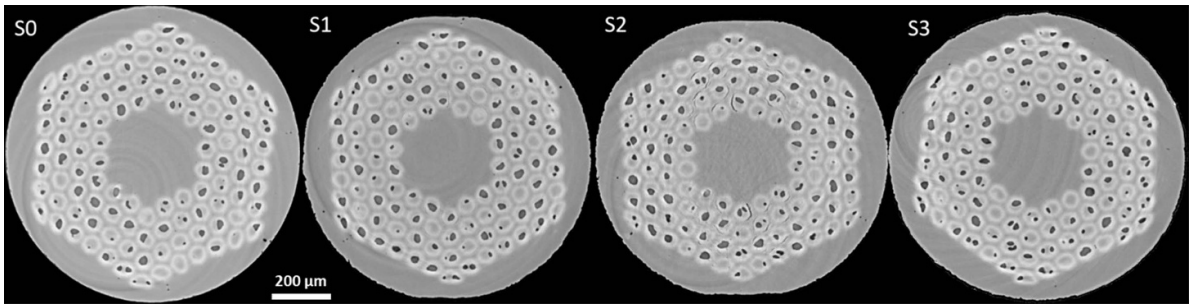

Figure 3. Tomographic cross section of the samples tested at ESRF. The effect of the different types of deformation is visible in S1 (1 kN pressed bare wire), S2 (2 kN pressed bare wire), S3 (wire in epoxy impregnation stressed at 238 MPa) compared to the non-deformed wire, S0.

features of superconducting wires in several studies [11, 29], allowing detection and definition of internal structures in a wire, such sub-elements, voids and cracks, without affecting the sample. The sample wire is exposed transversally to the x-ray beam, and the transmitted beam is captured by a detector situated behind a 360° rotating sample holder. In our case, a sample projection was acquired every 0.036°, which is equivalent to 10 000 projections per scan. These projections, once stacked into a 3D x-ray absorption map, are reconstructed to yield a 3D section of the sample volume. The photon energy was about 70–80 keV (filtered white beam) and the detector had 2560 × 2160 pixels resolution with an equivalent spatial sampling of about 0.7 μm pixel^{-1}. The analysed sample length during each scan is about 1.5 mm of wire, equivalent to 2160 horizontal slices per scan. Because C-WASP helicoidal samples have an equivalent internal diameter of ∼39 mm, the S3 and S4 segments had an evident curvature. This implies that not all the radiation from the x-ray beam reaches the sample orthogonally to the longitudinal wire direction. As a result, some of the reconstructed images may have aberrations since the reconstruction was generated starting from the barycentre of the sample volumes. Only tomographic data with no obvious aberrations were used in the following analysis for the detection of cracks. Table 2 lists the tomographic scans that were used in the current study.

3. Results and analysis

3.1. U-net training and validation

U-net was implemented in the python deep learning framework PyTorch [38]. Due to the small dataset needed by U-net, the training can be performed on a laboratory computer equipped with an NVIDIA graphics processing unit, in our case a model Quadro K1200, an entry-level card that showcases the low resource requirements of the neural network.

The U-net training goal was to teach the CNN to segment and separate cracks and voids from the other components of the wire. For this purpose, 20 tomographic images were selected from the first set of data, S1.1 and S2.1, i.e. the bare wires pressed with 1 and 2 kN of force. Cracks and voids were segmented from these images to produce the output examples. The cracks were manually detected one by one using GNU Image Manipulation Program [39], while the voids were segmented exploiting the TAT [31]. TAT is a machine learning application that uses pixel colour to segment tomographic images into clusters. The clusters provide a good baseline for the voids training after manual polishing of the TAT outputs. To serve as an output example, the segmented cracks and voids are saved on separate image layers with the same size and resolution as the original tomographic scans. Figure 4 depicts an example of input–output training in which only a portion of the entire tomography is displayed in order to better highlight cracks and voids. The input is displayed on the left as a section of the original wire tomography, while the output is shown on the right, as the identical image section with superimposed the two so-called 'masks' for cracks (in red) and voids (in cyan).

We used the data augmentation technique [40] to reduce the number of original examples needed and maximize the training efficiency. Data augmentation is essential to teach the network the desired invariance and robustness properties with only few training samples. Therefore, the input and output examples were rotated and transposed multiple times increasing the training pool of a factor 20, i.e. transforming 20 examples into 400. At the end of the training, the CNN tool was tested and validated.

After the training, U-net can identify voids and cracks in every wire tomography it analyses. The outputs consist of two distinct maps, one for each feature, with the other wire components being disregarded. The maps are empty when the neural network is unable to locate the specific feature that has been asked to detect. For example, when the trained CNN was applied to the tomographic images of S0.1, which is the wire without induced deformations, no cracks were observed, as expected. On the other hand, a considerable number of cracks were segmented in the tomographic images of the sample S1.1. To verify the quality of the detection, the voids and cracks maps were superimposed to the original tomography and manually checked for missing elements. Because manually inspecting all of the images, i.e. more than 2000 per sample, was impractical, a randomly selected subset was reviewed. Figure 5(a) shows an example of this superimposition, with the voids displayed in cyan and the cracks in red. After a visual inspection of the outputs, we were not able to find undetected cracks.

Furthermore, using an image processing software such as Fiji [41], it is possible to reconstruct the various components

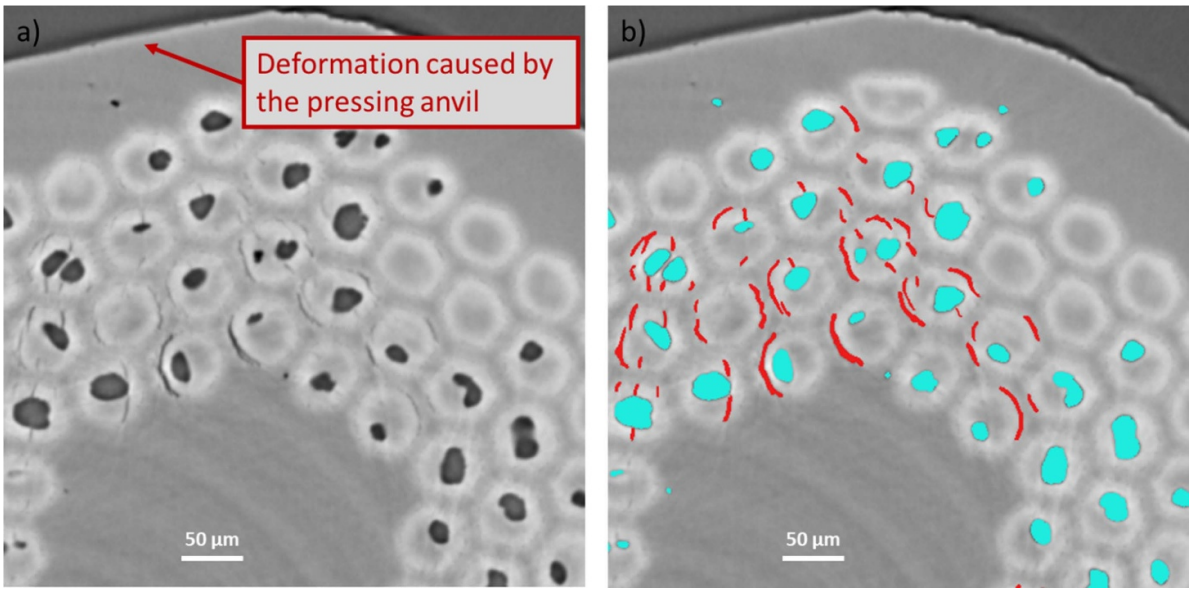

Figure 4. (a) Section of the tomography performed on the sample S2. (b) The result of the manual segmentation of the image with in red the cracks and in blue the sub-elements voids.

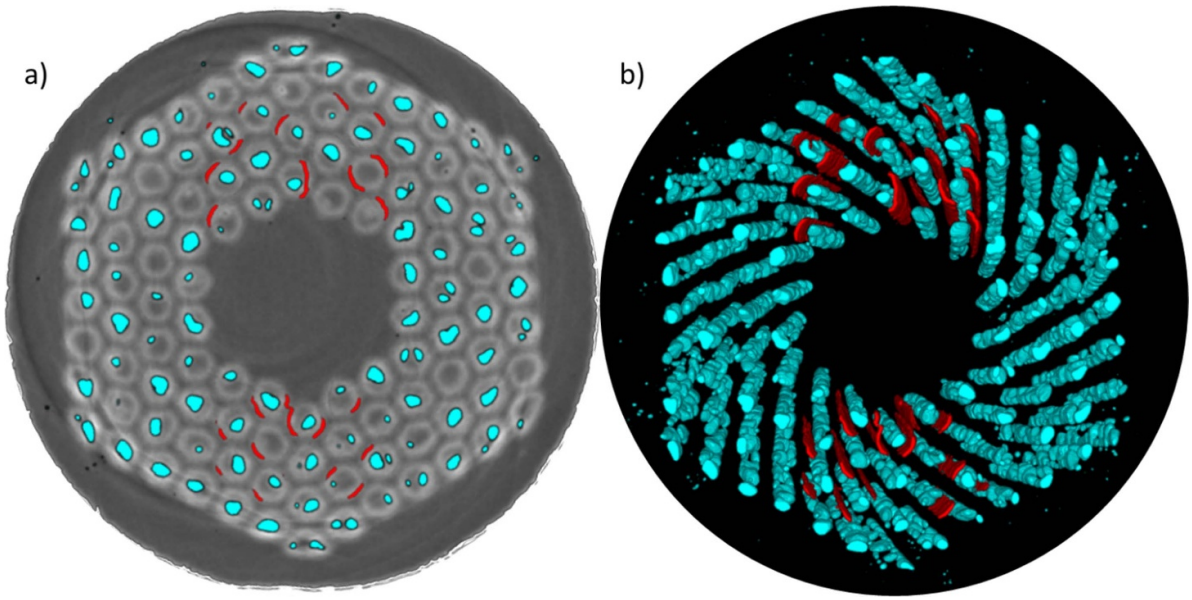

Figure 5. U-net verification test on sample S1.1. (a) The over imposition of the U-net outputs to the original tomography. (b) The 3D reconstruction of the U-net outputs. The voids are displayed in cyan while the cracks in red. The bare wire was transversally pressed with 1 kN of force.

in three dimensions (3Ds), providing a complete perspective of the cracks and voids and thus aiding in the detection of missing elements or sections, as shown in figure 5(b). In addition, the 3D map allows for direct observation of the properties of the sample, e.g. a rotation around the wire's centre of voids and cracks, which corresponds to the 14 mm twist pitch in the analysed wire.

3.2. Cracks and voids detection

The goal of the present research is to offer a method to investigate the presence of cracks in wires that underwent heavy stresses, like during magnet operation. In order to be analysed by tomography, S3 and S4 were extracted from an epoxy-impregnated wire sample at the end of a C-WASP experiment. The scans were performed on two different regions for each sample, providing a total of four tomographic datasets, see table 2. Of the four scans, the CNN detected cracks in S3.1, S3.2 and S4.1. The outputs of the analysis are displayed separately for these three samples.

Figure 6(a) shows a 3D reconstruction of S3.1 with the applied force direction marked, whereas figure 6(b) shows a 2D longitudinal cross section with voids and cracks displayed in red and cyan, respectively, in both pictures. The 3D image

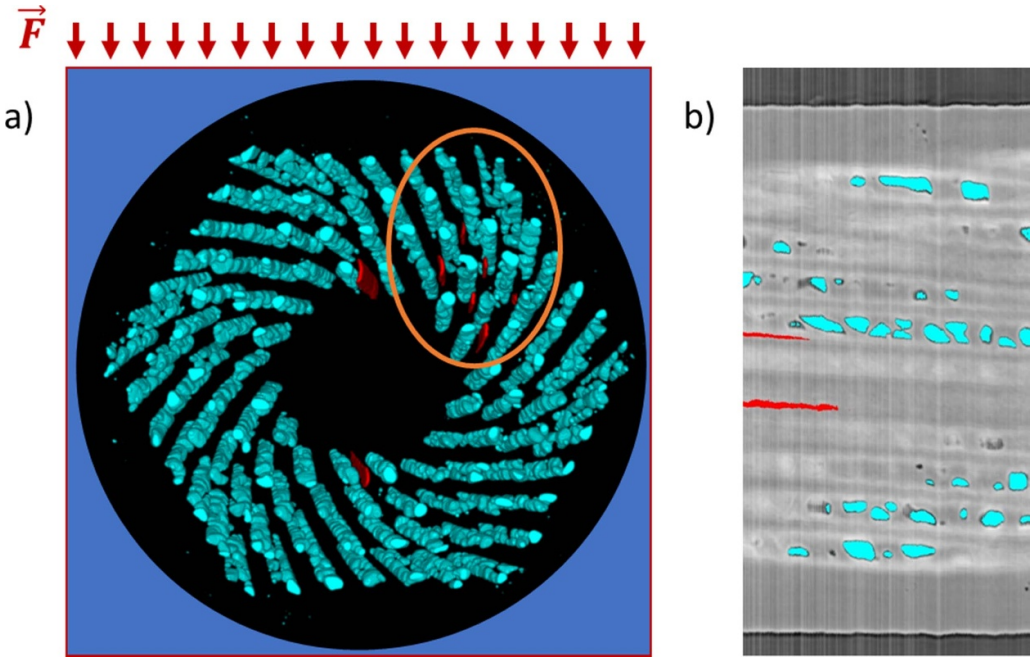

Figure 6. (a) The 3D reconstruction of the U-net output of S3.1. The applied force direction is depicted in green. (b) The 2D longitudinal cross section of S3.1 with superimposed the output of the CNN. The voids are displayed in cyan while the cracks in red.

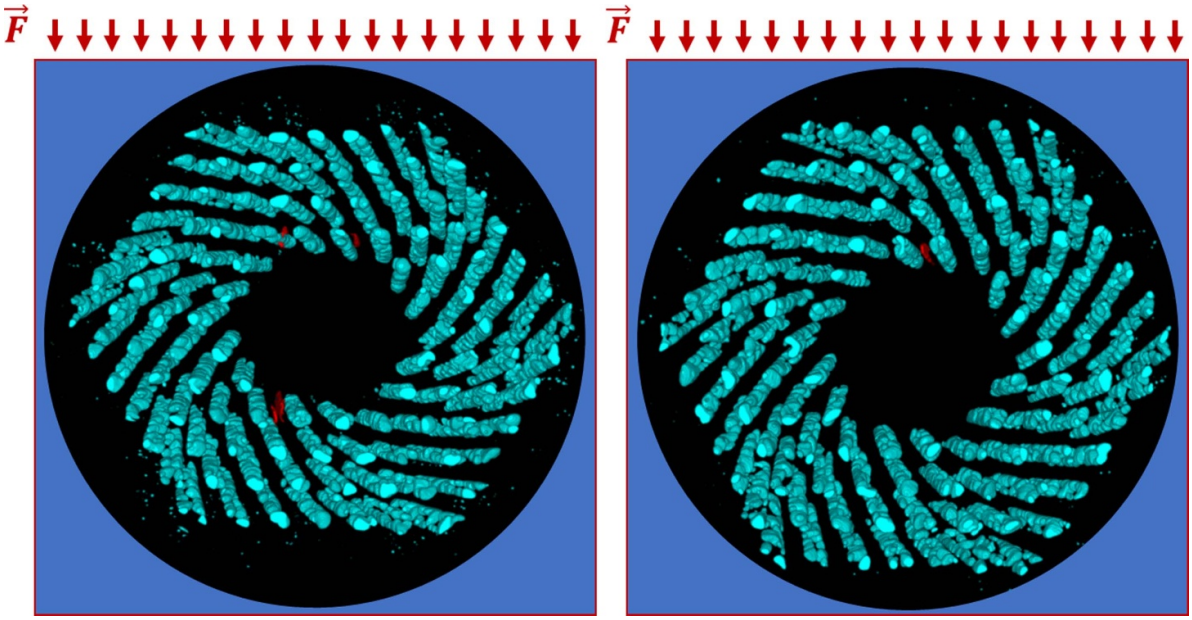

Figure 7. The 3D reconstructions of the U-net output of S3.2 and S4.1 are shown on the left and right, respectively. The voids are displayed in cyan while the cracks in red.

shows that the largest cracks are located in the innermost line of sub-elements. They are aligned to the force applied during the C-WASP test, and moreover they are longer than the region investigated in this tomographic volume, because no initiation nor termination of these cracks is visible in the tomographic images. Furthermore, there are six smaller cracks, underlined with the orange circle in figure 6(a), which end in the analysed section. In the longitudinal cross section, the terminations of two of these cracks are visible, they are located on the outer wall of the sub-elements and they do not seem to directly interact with Kirkendall voids.

The 3D reconstruction of voids and cracks in S3.2 and S4.1 are depicted in figure 7. These samples show less cracks than S3.1. The only detectable cracks are in the innermost sub-elements and aligned to the force applied on the C-WASP. As for S3.1, the cracks are at the interface between the sub-element and the copper matrix.

Furthermore, the 3D reconstruction of the voids can be used to statistically examine the variability in the voids dimension. Figure 8 depicts the distribution of voids as a function of their volume and in the different scans of the same sample. The voids with volume lower than 100 μm^3 are not

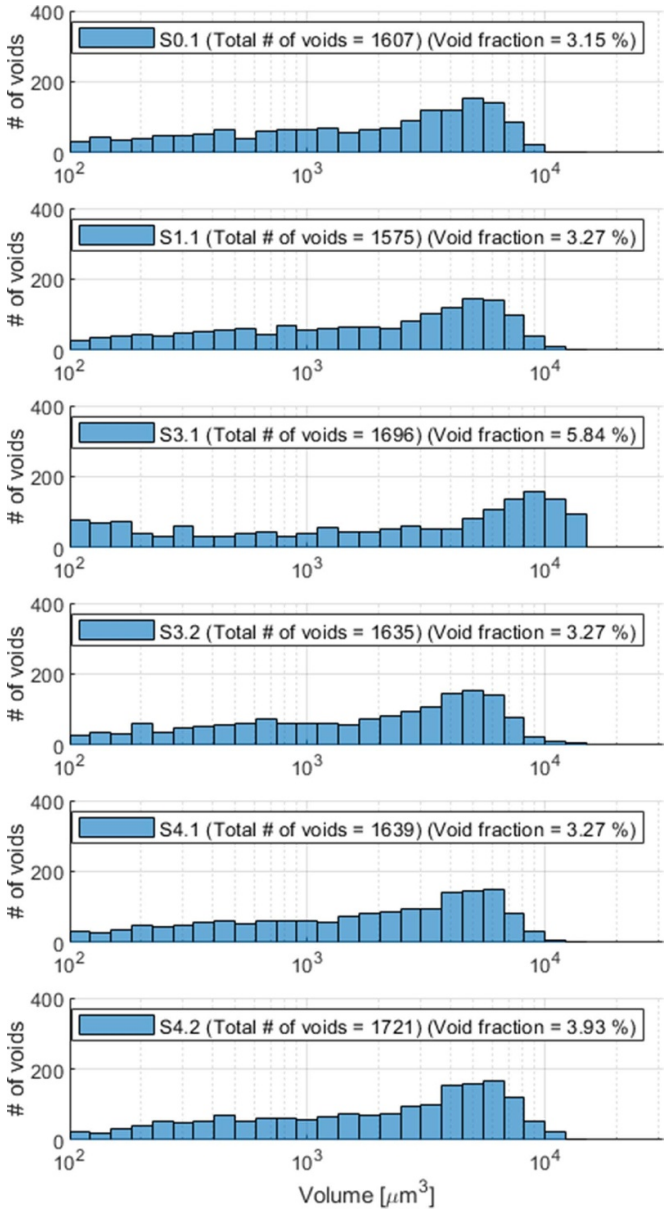

Figure 8. Distribution of the voids in the analysed samples as a function of volume. The total number of voids and the wire void fraction are reported in the legend of each graph.

considered in the distribution, since it was shown in [29] that voids smaller than this threshold are mostly located in the copper matrix and thus not affecting the mechanical behaviour of the wires. Moreover, sample S2.1 was excluded because the cracks crossed several of the voids affecting their size and shape, see figure 4. Except for S3.1, all samples show a similar void distribution, with void fractions ranging from 3.15% to 3.93% and comparable numbers of voids between 1575 and 1721. S3.1, however, has a higher void fraction of 5.84% despite showing a comparable number of voids, 1696. This suggests that some variability in the void dimensions can be present in RRP wires.

4. Discussion

The distribution of cracks detected in the wire after mechanical unloading from 238 MPa provides a number of interesting indications.

The cracks are mostly located in the innermost sub-elements, which implies that the inner sub-elements are more prone to damages. This result is in agreement with the study performed on the effect of RRP wire deformation on the sub-elements disruption in [42]. The study showed that the deformation, in that case performed before the reaction heat treatment, has a higher impact on the inner sub-elements. Furthermore, the same study pointed out that the 108/127 sub-elements distribution leaves the wire more prone to the stresses applied in correspondence of the corner of the hexagonal distribution of the sub-elements.

Numerical simulations of the C-WASP experiment showed that in case of a single wire with epoxy impregnation, the epoxy resin causes a partial redistribution of the applied stress over the wire surface, but the higher stress component is still parallel to the applied force direction and the maximal deformation is reached in the centre of the wire [10]. The simulations were carried out considering a measurement performed on a PIT Nb_3Sn wire but, the cracks detected in RRP wires, after the C-WASP measurement, are located in the innermost layer of the sub-elements and aligned with the applied force. This indicates that the degradation, due to transvers loads, starts in the centre for both wire types. Moreover, the cracks appear on the outer surface of the sub-elements at the interface with the copper matrix without propagating in the Nb_3Sn ring. Consequently, one can assume that copper matrix and rigid Nb_3Sn sub-elements can reach the point where the two components separate in the regions of the wire at the highest stresses. The type of cracks detected in our analysis could thus be a signature of this detachment.

Furthermore, the cracks propagate only longitudinally to the sub-elements. During the neural network analysis and the visual inspection of the outputs, no transversal cracks were detected. Only transversal cracks can be considered responsible for the I_c reduction because they interrupt the Nb_3Sn sub-elements reducing the total superconducting cross section of the wire and consequently the I_c. Therefore, the longitudinal cracks, detected in the examined volumes, do not justify the reduction of the 15% of the overall I_c measured during the C-WASP test. The cracks do not reduce the effective Nb_3Sn cross section, therefore the plastic deformation of the copper and the consequent B_{c2} reduction must be the major responsible for the critical current irreversible decrease in this type of wire when submitted to transverse loads. In a future publication, which is under preparation, it will be proven that the main reason for the I_c irreversible degradation on RRP wires is the copper plasticization [37]. These residual stresses are already relevant above 140 MPa, while cracks appear at far higher pressures in the range 200–250 MPa.

5. Conclusions

The degradation of 108/127 RRP Nb_3Sn wires was the subject of our case study. Two dedicated wire samples were deformed without impregnation at 1 kN and 2 kN of applied force to ensure the existence of cracks in the tomographic scans. The resulting tomographic images were used to train and validate U-net for this specific wire design. The training examples were prepared segmenting the cracks manually, while the voids were detected exploiting TAT. Following the validation, the analysis was carried out on two samples extracted from a 108/127 RRP Nb_3Sn wire at the end of a I_c versus transverse stress experiment, performed in the C-WASP probe at the University of Geneva. The wire was tested in epoxy impregnation up to 238 MPa of applied stress corresponding to 15% permanent degradation of the initial $I_{c,}$ after unloading the force. The CNN detected cracks localized at the innermost sub-elements of the wire, which corresponds to the highest stress region in the high purity copper matrix. The cracks propagate longitudinally without direct interaction with the Kirkendall voids in the sub-elements. Furthermore, since the longitudinal cracks do not interrupt the sub-elements limiting the superconducting cross section, they cannot be held fully responsible for the I_c reduction. Therefore, we can assess that the residual stresses on the Nb_3Sn caused by plastic deformation of the copper matrix is the main reason for the critical current degradation in this specific wire.

As a result of the study, we demonstrated the efficiency of combining U-net, a deep CNN, with x-ray tomography to detect and 3D reconstruct the internal features of Nb_3Sn wires. This type of analysis offers a more extensive and non-destructive investigation of the internal characteristics of a sample with respect to metallographic analyses. The proposed new method allows for a systematic approach in the understanding of the degradation phenomena of Nb_3Sn wires. Because of the small amount of examples required to train U-net, the tool can quickly adapt to diverse wire technologies and designs. Moreover, the 3D reconstruction of the features provides quantitative information on the wire internal characteristics, shedding light on the mechanical properties of Nb_3Sn wires and enabling researchers to develop new wires with improved mechanical tolerances.

Data availability statement

The data that support the findings of this study are available upon reasonable request from the authors.

Acknowledgments

This work was done under the auspices of CHART (Swiss Accelerator Research and Technology Collaboration, https://chart.ch).

Financial support was provided by the European Organization for Nuclear Research (CERN), Memorandum of Understanding for the FCC Study, Addendum FCC-GOV-CC-0176 (KE4612/ATS).

Research also supported by the European Synchrotron Radiation Facility (Grant No. MA-4604).

ORCID iDs

Tommaso Bagni https://orcid.org/0000-0001-8654-783X
Carmine Senatore https://orcid.org/0000-0002-9191-5016

References

[1] Matthias B T, Geballe T H, Geller S and Corenzwit E 1954 Superconductivity of Nb_3Sn *Phys. Rev.* **95** 1435
[2] Foner S and McNiff E J 1981 Upper critical fields of cubic and tetragonal single crystal and polycrystalline Nb_3Sn in DC fields to 30 tesla *Solid State Commun.* **39** 959–64
[3] Mitchell N, Bessette D, Gallix R, Jong C, Knaster J, Libeyre P, Sborchia C and Simon F 2008 The ITER magnet system *IEEE Trans. Appl. Supercond.* **18** 435–40
[4] Mitchell N and Devred A 2017 The ITER magnet system: configuration and construction status *Fusion Eng. Des.* **123** 17–25
[5] Apollinari G, Béjar Alonso I, Brüning O, Lamont M and Rossi L 2015 High-luminosity large hadron collider (HL-LHC): preliminary design report *Report No. CERN-2015-005, Medium: ED; Size: 19* (CERN)
[6] Baig T, Yao Z, Doll D, Tomsic M and Martens M 2014 Conduction cooled magnet design for 1.5 T, 3.0 T and 7.0 T MRI systems *Supercond. Sci. Technol.* **27** 125012
[7] Sharma R G 2021 *Superconductivity: Basics and applications to magnets* vol **214** (Switzerland: Springer Nature)
[8] Gan Z, Kwak H-T, Bird M, Cross T, Gor'kov P, Brey W and Shetty K 2008 High-field NMR using resistive and hybrid magnets *J. Magn. Reson.* **191** 135–40
[9] Barzi E and Zlobin A V 2019 *Nb_3Sn Accelerator Magnets: Designs, Technologies and Performance* ed D Schoerling and A V Zlobin (Switzerland: Springer International Publishing) pp 23–51
[10] Calzolaio C, Mondonico G, Ballarino A, Bordini B, Bottura L, Oberli L and Senatore C 2015 Electro-mechanical properties of PIT Nb_3Sn wires under transverse stress: experimental results and FEM analysis *Supercond. Sci. Technol.* **28** 055014
[11] Barth C, Seeber B, Rack A, Calzolaio C, Zhai Y, Matera D and Senatore C 2018 Quantitative correlation between the void morphology of niobium-tin wires and their irreversible critical current degradation upon mechanical loading *Sci. Rep.* **8** 6589
[12] Abada A *et al* 2019 FCC-hh: the hadron collider *Eur. Phys. J. Spec. Top.* **228** 755–1107
[13] Nijhuis A *et al* 2013 The effect of axial and transverse loading on the transport properties of ITER Nb_3Sn strands *Supercond. Sci. Technol.* **26** 084004
[14] Nijhuis A, Ilyin Y, Wessel S, Krooshoop E, Feng L and Miyoshi Y 2009 Summary of ITER TF Nb_3S strand testing under axial strain, spatial periodic bending and contact stress *IEEE Trans. Appl. Supercond.* **19** 1516–20
[15] Sheth M K, Lee P J, McRae D M, Sanabria C M, Starch W L, Walsh R P, Jewell M C, Devred A and Larbalestier D C 2012 Study of filament cracking under uniaxial repeated loading for ITER TF strands *IEEE Trans. Appl. Supercond.* **22** 4802504
[16] Nijhuis A, Miyoshi Y, Jewell M C, Abbas W and Wessel W A J 2009 Systematic study on filament fracture distribution in ITER Nb_3Sn strands *IEEE Trans. Appl. Supercond.* **19** 2628–32

[17] Sheth M K *et al* 2012 Procedures for evaluating filament cracking during fatigue testing of Nb_3Sn strand *AIP Conf. Proc.* **1435** 201–8
[18] Gutleber J *et al* 2015 EuroCirCol—Horizon 2020 research and innovation action *Report No. CERN-ACC-2018-0017* (CERN)
[19] Valente R, Bellomo G, Caiffi B, Fabbricatore P, Farinon S, Mariotto S, Pampaloni A, Ricci A M, Sorbi M and Statera M 2019 Baseline design of a 16 T cos θ bending dipole for the future circular collider *IEEE Trans. Appl. Supercond.* **29** 1–5
[20] Bordini B, Bottura L, Mondonico G, Oberli L, Richter D, Seeber B, Senatore C, Takala E and Valentinis D 2012 Extensive characterization of the 1 mm PIT Nb_3Sn strand for the 13-T FRESCA2 magnet *IEEE Trans. Appl. Supercond.* **22** 6000304
[21] Gämperle L, Ferradas J, Barth C, Bordini B, Tommasini D and Senatore C 2020 Determination of the electromechanical limits of high-performance Nb_3Sn Rutherford cables under transverse stress from a single-wire experiment *Phys. Rev. Res.* **2** 013211
[22] de Marzi G, Bordini B and Baffari D 2021 On the mechanisms governing the critical current reduction in Nb_3Sn Rutherford cables under transverse stress *Sci. Rep.* **11** 7369
[23] Troitino J F, Bagni T, Barth C, Bordini B, Ferracin P, Gamperle L, Tommasini D, Zurmuehle D and Senatore C 2021 Effects of the initial axial strain state on the response to transverse stress of high-performance RRP Nb_3Sn wires *Supercond. Sci. Technol.* **34** 035008
[24] Baffari D and Bordini B 2022 Effect of the sub-elements layout on the electro-mechanical properties of high J_c Nb_3Sn wires under transverse load: numerical simulations *IEEE Trans. Appl. Supercond.* **32** 1
[25] Kramer E J 1973 Scaling laws for flux pinning in hard superconductors *J. Appl. Phys.* **44** 1360–70
[26] Vander Voort G F 1986 *Applied Metallography* ed G F Vander Voort (Berlin: Springer) pp 139–70
[27] Scheuerlein C, di Michiel M and Haibel A 2007 On the formation of voids in internal tin Nb_3Sn superconductors *Appl. Phys. Lett.* **90** 132510
[28] Scheuerlein C, di Michiel M and Buta F 2009 Synchrotron radiation techniques for the characterization of Nb_3Sn superconductors *IEEE Trans. Appl. Supercond.* **19** 2653–6
[29] Bagni T, Bovone G, Rack A, Mauro D, Barth C, Matera D, Buta F and Senatore C 2021 Machine learning applied to x-ray tomography as a new tool to analyze the voids in RRP Nb_3Sn wires *Sci. Rep.* **11** 7767
[30] Haldi H, Bagni T and Mauro D 2021 *TAT* (available at: https://tat.readthedocs.io)
[31] Bagni T, Haldi H, Mauro D and Senatore C 2022 Tomography analysis tool: an application for image analysis based on unsupervised machine learning *IOP SciNotes* **3** 015201
[32] Ronneberger O, Fischer P and Brox T (Springer International Publishing) pp 234–41
[33] Stevens E, Antiga L and Viehmann T 2020 *Deep Learning with PyTorch* (United States of America: Manning Publications)
[34] Aghdam H H and Heravi E J 2017 *Guide to Convolutional Neural Networks* vol 10 (New York: Springer) p 51
[35] Shelhamer E, Long J and Darrell T 2017 Fully convolutional networks for semantic segmentation *IEEE Trans. Pattern Anal. Mach. Intell.* **39** 640–51
[36] Ferracin P *et al* 2016 Development of MQXF: the Nb_3Sn low-β quadrupole for the HiLumi LHC *IEEE Trans. Appl. Supercond.* **26** 1–7
[37] Bagni T and Senatore C 2022 Manuscript in preparation
[38] Paszke A *et al* 2017 Automatic differentiation in PyTorch
[39] The GIMP Development Team 2021 GIMP (available at: www.gimp.org/)
[40] Dosovitskiy A, Springenberg J T, Riedmiller M and Brox T 2014 Discriminative unsupervised feature learning with convolutional neural networks *Adv. Neural Inf. Process. Syst.* **27** 1–9
[41] Schindelin J *et al* 2012 Fiji: an open-source platform for biological-image analysis *Nat. Methods* **9** 676–82
[42] Polyanskii A A *et al* 2019 Evidence for highly localized damage in internal tin and powder-in-tube Nb_3Sn strands rolled before reaction obtained from coupled magneto-optical imaging and confocal laser scanning microscopy *Supercond. Sci. Technol.* **22** 095008